Journal of Magnetic Resonance 209 (2011) 291–299

Contents lists available at ScienceDirect

Journal of Magnetic Resonance

journal homepage: www.elsevier.com/locate/jmr

Homogeneous length scale of shear-induced multilamellar vesicles studied by diffusion NMR

Ingrid Åslund [a], Bruno Medronho [a,b], Daniel Topgaard [a], Olle Söderman [a], Claudia Schmidt [c,*]

[a] Physical Chemistry, Center of Chemistry and Chemical Engineering, Lund University, Box 124, 221 00 Lund, Sweden
[b] Department of Chemistry, University of Coimbra, 3004-535 Coimbra, Portugal
[c] Department of Chemistry, University of Paderborn, Warburger Straße 100, 33098 Paderborn, Germany

ARTICLE INFO

Article history:
Received 6 November 2010
Revised 19 January 2011
Available online 3 February 2011

Keywords:
Diffusion
Pulsed-gradient-spin-echo NMR
Lamellar phase
Shear

ABSTRACT

A recently developed protocol for pulsed gradient spin echo (PGSE) NMR is applied for the size determination of multilamellar vesicles (MLVs). By monitoring the self-diffusion behavior of water, the technique yields an estimate of the homogeneous length scale λ_{hom}, i.e. the maximum length scale at which there is local structural heterogeneity in a globally homogeneous material. A cross-over between local non-Gaussian to global Gaussian diffusion is observed by varying the experimentally defined length- and time-scales. Occasional observation of a weak Bragg peak in the PGSE signal attenuation curves permits the direct estimation of the MLV radius in favorable cases, thus yielding the constant of proportionality between λ_{hom} and radius. The microstructural origin of the Bragg peak is verified through Brownian dynamics simulations and a theoretical analysis based on the center-of-mass diffusion propagator. λ_{hom} is decreasing with increasing shear rate in agreement with theoretical expectations and results from ^{2}H NMR lineshape analysis.

1. Introduction

Multilamellar vesicles, MLVs, also known as onions, spherulites or liposomes, can be formed when shear is applied to a lamellar phase. When using steady shear at a constant rate the MLVs are fairly monodisperse in size and their radius can be controlled by the applied shear rate [1–3]. Since the first reports on such monodisperse shear-induced MLVs they have been found in many other lamellar systems [4–13]. Generally, the vesicle radius decreases with the shear rate; it is often approximately proportional to the square root of the inverse rate [2,14]. Sometimes the polydispersity of the MLV size is so low that periodic structures are formed [13,15–18]. However, the simple picture of densely packed spheres is misleading since there are no solvent-filled voids in the system; electron microscopy has shown that space is completely filled by the lamellar phase and that the onions have polyhedral shape [19]. Therefore, the onion structure is better characterized as a defect structure of the lamellar phase with a topology similar to that of a foam. A schematic picture is shown in Fig. 1.

Shear-induced MLVs can be metastable for a long time and the closed-shell structure of the bilayers allows for both hydrophilic and hydrophobic molecules to be trapped in the onions. Hence they may be useful, for instance, as carrier systems for drugs [20]. In addition, there is also a fundamental interest directed towards a physical understanding of the processes of onion formation and destruction and the elucidation of any intermediate structures during these processes [10,13,14,21–27].

One technique that can be used to investigate shear-induced structural changes of the lamellar phase is measurements of diffusion by NMR. Using flow-compensated multi-echo pulsed gradient NMR Lutti and Callaghan measured the diffusion spectra of lamellar samples under shear [28–32]. Based on models of the phase structure they could fit the experimental diffusion spectra and obtain structural parameters such as the onion dimensions at various shear rates [30].

Pulsed-gradient-spin-echo (PGSE) NMR is a well-established technique for studying structure and molecular transport in microheterogeneous systems in general [33–35]. The NMR signal is encoded for molecular displacements using pairs of magnetic field gradient pulses. The time and length scales, and also the direction in which motion is monitored, can be adjusted by varying the properties of the gradient pulse pair. Typically, molecular motion is studied on the $1-1000$ ms time scale and the 1–100 μm length scale. For bulk liquids the gradual spreading out of molecules from their starting position obeys Gaussian statistics and can be characterized with the bulk self-diffusion coefficient D_0. The low solubility of water in the hydrocarbon domains in a lamellar phase renders the water diffusion highly

* Corresponding author. Fax: +49 5251 604208.
E-mail addresses: ingrid.aslund@fkem1.lu.se (I. Åslund), bfmedronho@portugalmail.pt (B. Medronho), Daniel.Topgaard@fkem1.lu.se (D. Topgaard), olle.soderman@fkem1.lu.se (O. Söderman), claudia.schmidt@upb.de (C. Schmidt).

1090-7807/$ - see front matter © 2011 Elsevier Inc. All rights reserved.
doi:10.1016/j.jmr.2011.01.024

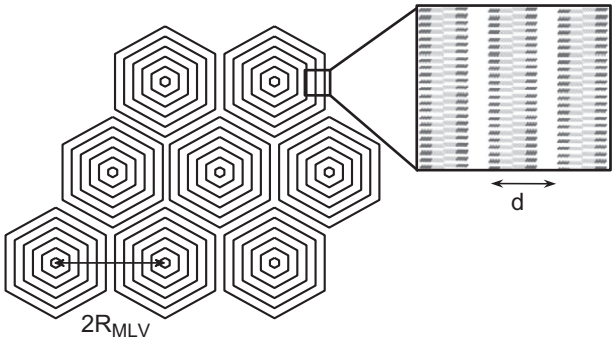

Fig. 1. Schematic two-dimensional (2D) picture of shear-induced surfactant multilamellar vesicles (MLVs), showing the ideal polyhedral arrangement of monodisperse MLVs. The lines indicate the surfactant bilayers, offering resistance to water diffusion due to the low solubility of water in a hydrocarbon phase. The magnification shows a schematic picture of the bilayers where light gray symbolizes the tail of the surfactant, dark gray areas symbolizes the heads and the white parts are the water areas in between the stacked bilayers. R_{MLV} is the MLV radius and d is the repeating distance of the bilayer stack.

anisotropic; the ratio between the diffusivities perpendicular to and parallel with the lamellar director is usually above 10 [36]. For a macroscopically aligned lamellar phase the experimentally observed diffusion coefficient depends on the angle between the lamellar director and the magnetic field gradient. Considering the schematic picture of the MLVs in Fig. 1, it is clear that the outcome of the PGSE NMR experiment will depend strongly on the scales of observation. When motion is followed on a length scale smaller than the onion radius R_{MLV}, a broad distribution of diffusion coefficients will be observed since each lamellar orientation with respect to the field gradient gives rise to a separate diffusion coefficient. At very long scales of observation, the molecules will sample all lamellar orientations and the effect of the local anisotropy is averaged, yielding an effective diffusion coefficient D_∞ describing the long-range diffusion in the globally isotropic medium. In a previous publication [37] some of us have described an experimental protocol for determining the length scale at which there is a cross-over from locally anisotropic to globally isotropic diffusion. This length scale is denoted the homogeneous length scale λ_{hom} in analogy with the parameter used to characterize microstructural heterogeneity through image analysis [38]. The concept of λ_{hom} can also be compared to the representative elementary volume (REV) used in the field of porous materials as the smallest volume in which the locally evaluated properties, e.g. porosity, are the same as the global ones [39]. The linear extension of the REV can be identified as λ_{hom}.

In this contribution, we demonstrate that λ_{hom}, which is obtained as a model-free parameter from a set of PGSE attenuation curves, can be used as a measure for the structural length scale of shear-induced MLVs. This is exemplified by a well-studied model system, the 40 wt% aqueous solution of the nonionic surfactant $C_{10}E_3$ [21,23,24,26,27,40–43]. Complementary characterization of the system is carried out with ^{2}H NMR [43]. PGSE NMR applied to MLV systems is explored in some detail, both with Brownian dynamics simulations and from a theoretical perspective. While the basic theory for PGSE NMR can be found in several textbooks and reviews, e.g. Refs. [33–35,44], we here derive the theory in a somewhat unconventional way based on the work of Mitra and Halperin [45], the reason being that the experimental observations for MLV systems can be conveniently explained using their concepts of the center-of-mass (COM) density and COM diffusion propagator as replacements for the more commonly used spin density and diffusion propagator.

2. Theoretical considerations

2.1. PGSE signal and center-of-mass displacements

A time-varying magnetic field gradient $\mathbf{g}(t)$ imparts a temporal and spatial dependence to the NMR precession frequency $\omega(\mathbf{r},t)$ according to

$$\omega(\mathbf{r},t) = -\gamma \mathbf{g}(t)\cdot\mathbf{r}, \tag{1}$$

where γ is the magnetogyric ratio (2.675×10^8 rad/Ts for ^{1}H) and $\mathbf{r}$ is the position. Consider a nuclear spin performing a random walk $\mathbf{r}(t)$ in the time interval from $t = 0$ to $t = \tau$. The time-dependent phase $\phi(t)$ is at $t = \tau$ given by

$$\phi(\tau) = \int_0^\tau \omega(t)dt = -\gamma\int_0^\tau \mathbf{g}(t)\cdot\mathbf{r}(t)dt \tag{2}$$

if $\phi(0) = 0$. The NMR signal $E(t)$ results from the ensemble average

$$E(t) = \langle e^{i\phi(t)}\rangle. \tag{3}$$

In the pulsed gradient spin echo (PGSE) experiment, the NMR signal is encoded for molecular displacements employing two magnetic field gradient pulses of equal amplitude and direction, but opposite effective polarity. We can in Eq. (2) separate the gradient temporal profile $f(t)$ and the gradient vector $\mathbf{g}$, thus making the substitution $\mathbf{g}(t) \to \mathbf{g}f(t)$, yielding

$$\phi(\tau) = -\gamma\mathbf{g}\cdot\int_0^\tau f(t)\mathbf{r}(t)dt. \tag{4}$$

With pulse duration δ and separation Δ between the onset of the pulses, $f(t)$ is given by

$$f(t) = -H(t) + H(t-\delta) + H(t-\Delta) - H(t-\Delta-\delta), \tag{5}$$

as shown in Fig. 2. In Eq. (5), $H(t)$ is the Heaviside step function. Insertion of Eq. (5) into Eq. (4) yields

$$\phi(\Delta+\delta) = -\gamma\mathbf{g}\cdot\left(-\int_0^\delta \mathbf{r}(t)dt + \int_\Delta^{\Delta+\delta}\mathbf{r}(t)dt\right), \tag{6}$$

which can be rearranged to

$$\phi(\Delta+\delta) = -\gamma\mathbf{g}\delta\cdot\left(\frac{1}{\delta}\int_\Delta^{\Delta+\delta}\mathbf{r}(t)dt - \frac{1}{\delta}\int_0^\delta \mathbf{r}(t)dt\right). \tag{7}$$

Defining $\mathbf{r}'(t_1,t_2)$ as the center-of-mass (COM) of the random walk $\mathbf{r}(t)$ in the time interval $t_1 < t < t_2$ according to

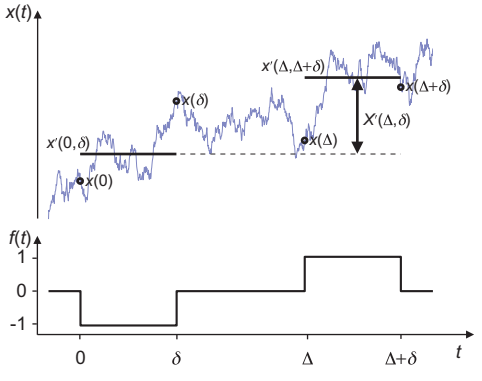

Fig. 2. Trajectory $x(t)$ for a random walker projected onto one dimension (top) and gradient temporal profile $f(t)$ of the PGSE NMR experiment according to Eq. (5) (bottom). Dots in the top panel indicate the positions $x(t)$ of the walker at the time points $t = 0$, δ, Δ, and $\Delta+\delta$. Solid lines in the top panel show the trajectory center-of-mass (COM) $x'(t_1,t_2)$ in the time intervals $(t_1,t_2) = (0,\delta)$ and $(\Delta,\Delta+\delta)$, see Eq. (8). The COM displacement $X'(\Delta,\delta)$, defined in Eq. (11), is indicated with a double arrow.

$$\mathbf{r}'(t_1,t_2)=\frac{1}{|t_2-t_1|}\int_{t_1}^{t_2}\mathbf{r}(t)dt \tag{8}$$

and the wave vector $\mathbf{q}$ as

$$\mathbf{q}=\frac{\gamma\mathbf{g}\delta}{2\pi}, \tag{9}$$

Eq. (7) can be written as

$$\phi(\Delta+\delta)=-2\pi\mathbf{q}\cdot[\mathbf{r}'(\Delta,\Delta+\delta)-\mathbf{r}'(0,\delta)]. \tag{10}$$

Let $\mathbf{R}'(\Delta,\delta)$ denote the COM displacement, i.e. the distance between the COMs of $\mathbf{r}(t)$ in the intervals $\Delta < t < \Delta+\delta$ and $0 < t < \delta$,

$$\mathbf{R}'(\Delta,\delta)=\mathbf{r}'(\Delta,\Delta+\delta)-\mathbf{r}'(0,\delta). \tag{11}$$

A one-dimensional trajectory, with COM positions and displacement indicated, is displayed in Fig. 2.

Combining Eqs. (3), (10) and (11) yields

$$E(\Delta+\delta)=\langle e^{-i2\pi\mathbf{q}\cdot\mathbf{R}'(\Delta,\delta)}\rangle \tag{12}$$

for the signal in the end of the PGSE experiment, $t=\Delta+\delta$. In order to calculate the PGSE signal using Eq. (12), we need the probability distribution of $\mathbf{R}'$. Let us denote this quantity as the "COM displacement probability", $\overline{P}'(\mathbf{R},\Delta,\delta)$. Now writing the PGSE signal as a function of $\mathbf{q}$, Δ, and δ, Eq. (12) can be expressed as

$$E(\mathbf{q},\Delta,\delta)=\int\overline{P}'(\mathbf{R},\Delta,\delta)e^{-i2\pi\mathbf{q}\cdot\mathbf{R}}d\mathbf{R}. \tag{13}$$

Eq. (13) can be recognized as a Fourier transform with the conjugate variables $\mathbf{q}$ and $\mathbf{R}$.

2.2. Free diffusion

For diffusion with the self-diffusion coefficient D in an isotropic and homogeneous medium, both $\overline{P}'(\mathbf{R},\Delta,\delta)$ and $E(\mathbf{q},\Delta,\delta)$ are Gaussian:

$$\overline{P}'(\mathbf{R},\Delta,\delta)=[4\pi^2D(\Delta-\delta/3)]^{-3/2}e^{-\mathbf{R}\cdot\mathbf{R}/4D(\Delta-\delta/3)} \tag{14}$$

$$E(\mathbf{q},\Delta,\delta)=e^{-4\pi^2\mathbf{q}\cdot\mathbf{q}D(\Delta-\delta/3)} \tag{15}$$

The factor $(\Delta-\delta/3)$ in Eqs. (14) and (15) can be used to define an effective diffusion time t_d through

$$t_d=\Delta-\delta/3. \tag{16}$$

2.3. Closed pores

The diffusion propagator $P(\mathbf{r}_0|\mathbf{r},\tau)$, i.e. the probability density for spin displacement from $\mathbf{r}_0$ to $\mathbf{r}$ over the time interval τ, is often used to describe diffusion in a pore space. Apart from the case of free diffusion, analytical expressions for $P(\mathbf{r}_0|\mathbf{r},\tau)$ are known only for simple closed geometries such as cylinders and spheres [46–49]. The probability distribution of displacements $\mathbf{R}=\mathbf{r}-\mathbf{r}_0$, the "average propagator" $\overline{P}(\mathbf{R},\tau)$, is given by integration over all starting positions, weighted with local spin density $\rho(\mathbf{r}_0)$, according to

$$\overline{P}(\mathbf{R},\tau)=\int\rho(\mathbf{r}_0)P(\mathbf{r}_0|\mathbf{r}_0+\mathbf{R},\tau)d\mathbf{r}_0. \tag{17}$$

When the PGSE experiment is performed in the limit as $\delta\to 0$, then $\overline{P}(\mathbf{R},\Delta)$ can replace $\overline{P}'(\mathbf{R},\Delta,\delta)$ in Eq. (13). For spins diffusing in a closed pore space, $P(\mathbf{r}_0|\mathbf{r},\tau)$ becomes independent of $\mathbf{r}_0$ in the limit $\tau\to\infty$; the spin "loses memory" of its initial position. In this case $P(\mathbf{r}_0|\mathbf{r},\tau)=\rho(\mathbf{r})$, and $\overline{P}(\mathbf{R},\infty)$ is the autocorrelation function of $\rho(\mathbf{r})$ which we denote $\tilde{\rho}(\mathbf{R})$:

$$\overline{P}(\mathbf{R},\infty)=\int\rho(\mathbf{r})\rho(\mathbf{r}+\mathbf{R})d\mathbf{r}=\tilde{\rho}(\mathbf{R}). \tag{18}$$

Let us define a COM propagator $P'(\mathbf{r}_0|\mathbf{r},\tau)$, being the probability density for a spin starting at $\mathbf{r}_0$ having the COM position $\mathbf{r}'=\mathbf{r}$ over the time interval τ. Averaging over all starting positions yields the COM density $\rho'(\mathbf{r},\tau)$according to

$$\rho'(\mathbf{r},\tau)=\int\rho(\mathbf{r}_0)P'(\mathbf{r}_0|\mathbf{r},\tau)d\mathbf{r}_0. \tag{19}$$

In analogy with Eq. (18), $\overline{P}'(\mathbf{R},\Delta,\delta)$ is in the limit $\Delta\to\infty$ given by [45]

$$\overline{P}'(\mathbf{R},\infty,\delta)=\int\rho'(\mathbf{r},\delta)\rho'(\mathbf{r}+\mathbf{R},\delta)d\mathbf{r}=\tilde{\rho}'(\mathbf{R},\delta) \tag{20}$$

for closed pores. $E(\mathbf{q},\infty,\delta)$ is the Fourier transform of $\overline{P}'(\mathbf{R},\infty,\delta)$, which is the autocorrelation function of $\rho'(\mathbf{r},\delta)$. Then, according to the Wiener-Khinchin theorem, $E(\mathbf{q},\infty,\delta)$ is the power spectral density of $\rho'(\mathbf{r},\delta)$:

$$E(\mathbf{q},\infty,\delta)=|S'(\mathbf{q},\delta)|^2, \tag{21}$$

where $S'(\mathbf{q},\delta)$ denotes the Fourier transform of $\rho'(\mathbf{r},\delta)$. To summarize, Eq. (21) states that the PGSE signal $E(\mathbf{q},\infty,\delta)$ is the "diffraction pattern" of the COM density $\rho'(\mathbf{r},\delta)$, which is equal to the true spin density $\rho(\mathbf{r})$ in the limit $\delta\to 0$.

2.4. Microheterogeneous medium

Now consider a microscopically heterogeneous, but macroscopically isotropic and homogeneous, material with local spin density $\rho(\mathbf{r})$ and local diffusion tensor $\mathbf{D}(\mathbf{r})$, e.g. the MLV system of interest here. All variations of $\rho(\mathbf{r})$ and $\mathbf{D}(\mathbf{r})$ occur on a length scale smaller than the homogeneous length scale λ_{hom}. In the limit $\Delta\to\infty$, such that the typical displacement during Δ is much larger than λ_{hom}, we expect $\overline{P}'(\mathbf{R},\Delta,\delta)$ to be Gaussian, with a width given by an effective, long-range self-diffusion coefficient D_∞, modulated by $\tilde{\rho}'(\mathbf{R},\delta)$ [45]:

$$\overline{P}'(\mathbf{R},\Delta,\delta)=\tilde{\rho}'(\mathbf{R},\delta)[4\pi D_\infty(\Delta-\delta/3)]^{-3/2}e^{-\mathbf{R}\cdot\mathbf{R}/4D_\infty(\Delta-\delta/3)} \tag{22}$$

Note that the factor originating from the COM density is a function of δ, while the Gaussian envelope depends on $t_d=\Delta-\delta/3$. Changing δ at constant t_d leads to a modulation of $\overline{P}'(\mathbf{R},\Delta,\delta)$ on a length scale smaller than λ_{hom}, while preserving the overall Gaussian shape.

Fourier transform of Eq. (22) yields

$$E(\mathbf{q},\Delta,\delta)=|S'(\mathbf{q},\delta)|^2\otimes e^{-4\pi^2\mathbf{q}\cdot\mathbf{q}D_\infty(\Delta-\delta/3)}, \tag{23}$$

where $\otimes$ denotes a convolution. Variation of $\overline{P}'(\mathbf{R},\Delta,\delta)$ on length scales smaller than λ_{hom} for constant overall shape corresponds to a variation of $E(\mathbf{q},\Delta,\delta)$ at values of q larger than $1/\lambda_{\mathrm{hom}}$. As suggested and demonstrated in a previous publication [37], and further demonstrated with Brownian dynamics simulations below, the smallest value of q for which E is changing when varying δ at constant $\Delta-\delta/3$ can be used to estimate λ_{hom}.

In cases where the displacement probability and PGSE signal depend on t_d rather than Δ, it is more convenient to write them as functions of t_d and δ. Such notation will be used for the remainder of this paper.

3. Brownian dynamics simulations

3.1. Simulation details

A two-dimensional model of the MLV phase is shown in Fig. 3. The unit cell of the periodic structure is a single MLV, which consists of a central core, a middle layer, and an outer layer. A square lattice, with distance dx between adjacent lattice points, defines the allowed positions of the random walkers. The distance between the centers of neighboring MLVs is $2R_{\mathrm{MLV}}=5\mathrm{d}x$. For each

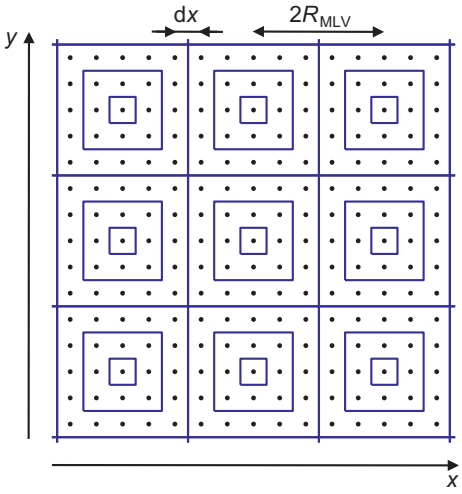

Fig. 3. Two-dimensional "square onion" geometry used in the simulation of displacement probabilities and PGSE signal. The square grid of black points with separation dx shows the allowed positions of the random walkers in the x,y-plane. Blue lines indicate the MLV layers. The centers of adjacent MLVs are separated by a distance $2R_{MLV} = 5dx$. The geometry is periodic and extends indefinitely in the x and y directions.

time step dt, a random number determines if the walker takes a step to one of the four nearest neighboring lattice points, or stays at the starting point. A jump between lattice points within the same layer occurs with the probability $P_{\parallel}$, while a step across layer boundaries has the probability $P_{\perp}$. The jump probabilities are related to the diffusion coefficients parallel and perpendicular to the layers, $D_{\parallel}$ and $D_{\perp}$, via $D_{\parallel/\perp} = P_{\parallel/\perp}dx^2/dt$. A total of 2.5×10^5 walkers were released at the 25 lattice points in the central unit cell, and their trajectories $\mathbf{r}(t)$ during 10^4 time steps were stored for further analysis. The propagator $P(\mathbf{r}_0|\mathbf{r},\tau)$, the COM propagator $P'(\mathbf{r}_0|\mathbf{r},\tau)$, and the COM displacement probability $\overline{P'}(\mathbf{R},t_d,\delta)$ were evaluated by first calculating the COM positions $\mathbf{r}'$ and displacements $\mathbf{R}'$ with Eqs. (8) and (11), and then constructing two-dimensional histograms using the lattice points as centers of the bins. The COM density $\rho'(\mathbf{r},\tau)$ was calculated with Eq. (19) and the PGSE signal $E(\mathbf{q},t_d,\delta)$ was evaluated using Eq. (12) for 256 geometrically spaced q-values. Values of δ and t_d are reported in the figure captions.

The simulations were implemented in MATLAB R2009b on a Mac with double 2.26 GHz Quad-Core Intel Xeon processors, 6 GB RAM, and 64-bit operating system. With the simulations running in the background on a single processor core, the entire set of data presented here required about one hour of CPU time.

3.2. Probability distributions

In Fig. 4 simulated $P(\mathbf{r}_0|\mathbf{r},\tau)$, $P'(\mathbf{r}_0|\mathbf{r},\tau)$, and COM density $\rho'(\mathbf{r},\tau)$ are displayed. A system where the walkers cannot cross the boundaries between the layers ($P_{\perp} = 0$ and $P_{\parallel} = 0.25$) is shown in Fig. 4a. In the top row, $P(\mathbf{r}_0|\mathbf{r},\tau)$ illustrates the gradual spreading of the walkers from the starting position $\mathbf{r}_0$ (labeled with a red box) to an even distribution in the outer layer of the central MLV at long τ.

While $P(\mathbf{r}_0|\mathbf{r},\tau)$ shows where the walkers are at the instant $t = \tau$, $P'(\mathbf{r}_0|\mathbf{r},\tau)$, in the second row of Fig. 4a, shows the COMs of the paths taken by the walkers in the time interval $0 < t < \tau$. $P'(\mathbf{r}_0|\mathbf{r},\tau)$ is a δ-function at $\mathbf{r}_0$ for small τ, spreads out and moves toward the center of the MLV with increasing τ, and finally becomes a δ-function in the center of the MLV for long τ. At such long τ, each random walker starting at $\mathbf{r}_0$ has explored the entire outer layer repeatedly, thus having a COM of the trajectory in the very middle of the MLV. The spin phase ϕ acquired during the first gradient pulse of the PGSE

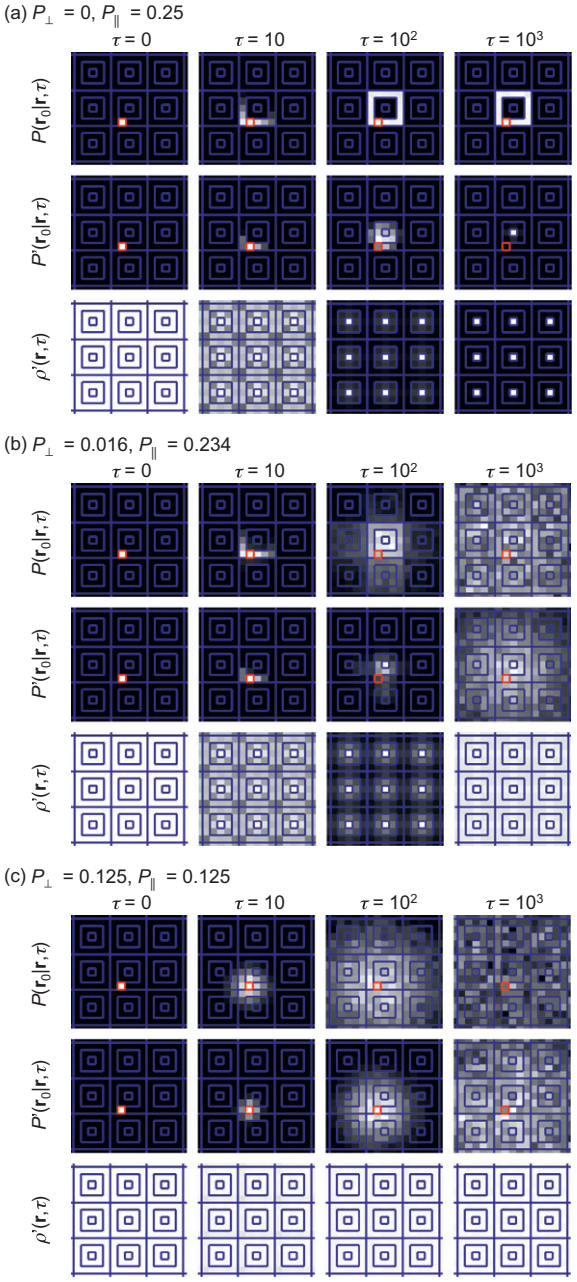

Fig. 4. Simulated propagator $P(\mathbf{r}_0|\mathbf{r},\tau)$, COM propagator $P'(\mathbf{r}_0|\mathbf{r},\tau)$, and COM density $\rho'(\mathbf{r},\tau)$ for the "2D square onion" geometry (see Fig. 3) as a function of position $\mathbf{r} = (x,y)$ and time τ (given in units of the simulation time step dt). Blue lines show the MLV layers and the red square indicates the initial position $\mathbf{r}_0$ of the random walkers when simulating $P(\mathbf{r}_0|\mathbf{r},\tau)$ and $P'(\mathbf{r}_0|\mathbf{r},\tau)$. Data is shown for three levels of anisotropy: (a) high anisotropy, $P_{\perp} = 0$ and $P_{\parallel} = 0.25$, (b) low anisotropy, $P_{\perp} = 0.016$ and $P_{\parallel} = 0.234$, (c) isotropic, $P_{\perp} = P_{\parallel} = 0.125$, where $P_{\perp/\parallel}$ is the probability of taking a step across/along an MLV layer boundary for each time step. The grayscale is linear between zero (black) and the maximum value (white), being rescaled for each subfigure. (For interpretation of the references to colour in this figure legend, the reader is referred to the web version of this article.)

experiment is a label of the COM of the path during the application of the pulse. As illustrated with $P(\mathbf{r}_0|\mathbf{r},\tau)$ and $P'(\mathbf{r}_0|\mathbf{r},\tau)$ at long τ, the spins starting in the outer layer of the MLV will acquire a phase label characteristic for the MLV center, although not a single one of them has actually been there.

The bottom row in Fig. 4a shows $\rho'(\mathbf{r},\tau)$, which equals $P'(\mathbf{r}_0|\mathbf{r},\tau)$ averaged over all starting positions according to Eq. (19). The importance of $\rho'(\mathbf{r},\tau)$ lies in the straightforward relation between

its Fourier transform and the PGSE signal, see Eqs. (21) and (23). With increasing τ, $\rho'(\mathbf{r},\tau)$ changes from being independent of $\mathbf{r}$ to a set of δ-functions at the MLV centers. Since the Fourier transform of a periodic set of δ-functions in real space is another set of δ-functions in reciprocal space, these results show that the PGSE signal may display Bragg peaks related to the distance between MLV centers. It is worth emphasizing that the periodicity of the COM density $\rho'(\mathbf{r},\tau)$ originates from the periodicity of the local diffusion tensor $\mathbf{D}(\mathbf{r})$ while the true spin density $\rho(\mathbf{r})$ is homogeneous.

Results from a system with finite permeability across the layer boundaries ($P_\perp = 0.016$ and $P_\parallel = 0.234$) are shown in Fig. 4b. Also in this case $P(\mathbf{r}_0|\mathbf{r},\tau)$ initially spreads along the outer layer in which $\mathbf{r}_0$ is located, but at later times moves into the inner layers and adjacent MLVs. At even longer τ, $P(\mathbf{r}_0|\mathbf{r},\tau)$ assumes an overall Gaussian shape. Since $P(\mathbf{r}_0|\mathbf{r},\tau)$ initially follows the MLV layers, $P'(\mathbf{r}_0|\mathbf{r},\tau)$ moves towards the MLV center, although the effect is not as pronounced as for the $P_\perp = 0$ case. At long τ, $P'(\mathbf{r}_0|\mathbf{r},\tau)$ extends far beyond the limits of the MLV in which $\mathbf{r}_0$ is located. Hence, uniform $\rho'(\mathbf{r},\tau)$ are obtained in both the short- and long-τ limits. Maximally peaked $\rho'(\mathbf{r},\tau)$ at the MLV centers are obtained for intermediate values of τ.

As a reference, results from an isotropic system ($P_\perp = P_\parallel = 0.125$) are displayed in Fig. 4c. Both $P(\mathbf{r}_0|\mathbf{r},\tau)$ and $P'(\mathbf{r}_0|\mathbf{r},\tau)$ are Gaussian having widths increasing with τ. Since the medium is homogeneous with respect to both $\mathbf{D}(\mathbf{r})$ and $\rho(\mathbf{r})$, $\rho'(\mathbf{r},\tau)$ remains constant irrespective of the value of τ.

3.3. PGSE signal

Fig. 5 shows simulated $\rho'(x,\delta)$, $\overline{P}'(X,t_d,\delta)$, and $E(q,t_d,\delta)$ for a system with $P_\perp = 0.016$ and $P_\parallel = 0.234$. $\rho'(x,\delta)$ equals the projection of $\rho'(\mathbf{r},\tau)$ in Fig. 4b onto the x-axis. Increasing δ from 10dt (blue) to 100dt (red) leads to sharper peaks at the MLV centers, $x/2R_{MLV} = 0, \pm 1, \pm 2, \ldots$. According to Eq. (22), $\overline{P}'(X,t_d,\delta)$ in Fig. 5b equals the autocorrelation function of $\rho'(\mathbf{r},\tau)$ weighted with a Gaussian corresponding to the long-range diffusion. Increasing δ from 10dt (blue) to 100dt (red) at constant $t_d = \Delta - \delta/3$, either $114\frac{2}{3}$dt (dashed) or $349\frac{2}{3}$dt (solid), leads to a small-scale modulation of $\overline{P}'(X,t_d,\delta)$ while preserving the Gaussian envelope, the width of which is proportional to $t_d^{1/2}$.

The modulation of $\overline{P}'(X,t_d,\delta)$ is even more visible in its Fourier transform, $E(q,t_d,\delta)$ in Fig. 5c. The q-range can be divided into two regions with respect to the effect of varying δ at constant t_d. At low q, $E(q,t_d,\delta)$ is decaying faster for longer t_d, but is independent of δ as expected for a homogeneous medium, see Eq. (15). An apparent diffusion coefficient $D(t_d,\delta)$ can be estimated by fitting Eq. (15) to the low-q part of the data [37]. With increasing t_d and δ, $D(t_d,\delta)$ approaches the long-time value D_∞. The variation of $E(q,t_d,\delta)$ at high q corresponds to the small-scale modulation of $\overline{P}'(X,t_d,\delta)$. The border between the two regions of q, indicated with the vertical line in Fig. 5c, defines the homogeneous length scale λ_{hom}, i.e. the smallest length scale at which the material appears homogeneous. A numerical estimate of λ_{hom} is obtained by evaluating the ratio between the highest and lowest values of $E(q,t_d,\delta)$ when varying δ at constant t_d and q. The largest value of q for which this ratio is below a certain threshold is taken as the inverse of λ_{hom} [37]. Here we have chosen to use a threshold value of 1.1. Increasing the threshold value makes the analysis more robust with respect to the influence of experimental noise at the expense of inducing systematic deviations.

The Bragg peak in $E(q,t_d,\delta)$ at $q\cdot 2R_{MLV} = 1$ for $\delta = 100$dt and $t_d = 349\frac{2}{3}$dt (red, solid), shown with the arrow in Fig. 5c, corresponds to the set of local maxima of $\overline{P}'(X,t_d,\delta)$ at $X/2R_{MLV} = 0, \pm 1, \pm 2, \ldots$, originating from the local maxima of $\rho'(x,\delta)$ at $x/2R_{MLV} = 0, \pm 1, \pm 2, \ldots$. The amplitude of the Bragg peak can be maximized by choosing an optimum value of δ for which the maxima of $\rho'(\mathbf{r},\delta)$, as shown in Fig. 4b, are as sharp as possible. For the Bragg peak to be visible, t_d has to be long enough for the envelope of $\overline{P}'(X,t_d,\delta)$ to cover a range of at least a few R_{MLV}. Thus, for favorable choices of δ and t_d the MLV radius R_{MLV} can be directly deduced from the position of the Bragg peak.

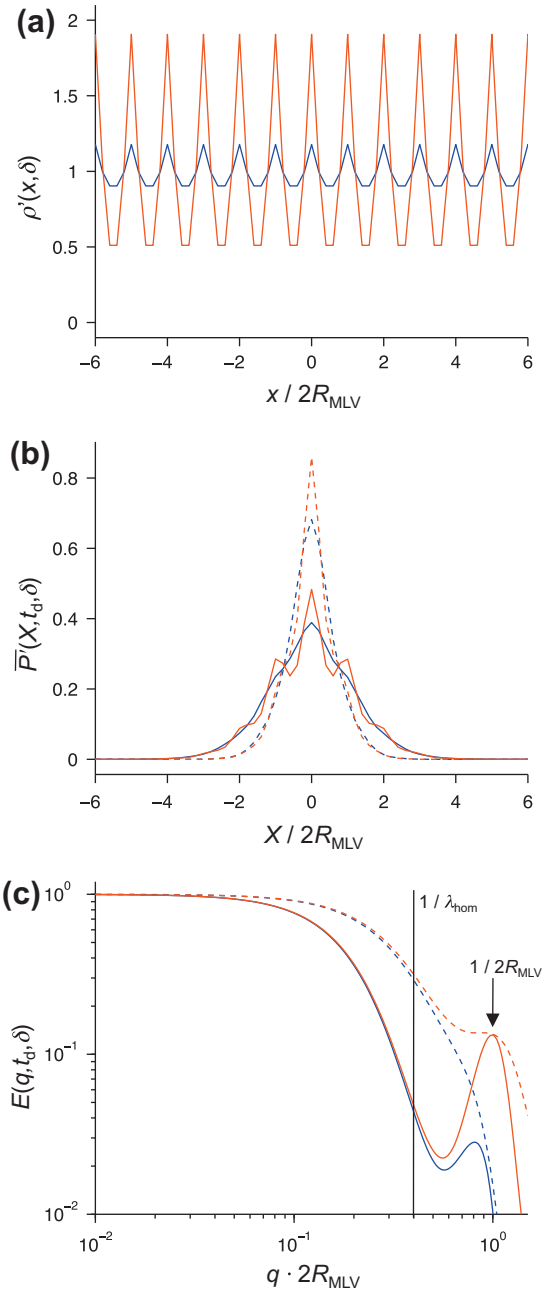

Fig. 5. Simulation results for the "2D square onion" geometry in Fig. 3 with $P_\perp = 0.016$ and $P_\parallel = 0.234$. (a) COM density $\rho'(x,\delta)$ vs. position x for the gradient pulse lengths $\delta = 10$ (blue) and 100 (red). (b) COM displacement probability $\overline{P}'(X,t_d,\delta)$ vs. displacement X for $\delta = 10$ (blue) and 100 (red), and effective diffusion times $t_d = \Delta - \delta/3 = 114\frac{2}{3}$ (dashed) and $349\frac{2}{3}$ (solid). (c) PGSE signal $E(q,t_d,\delta)$ vs wave vector q for $\delta =$ 10 (blue) and 100 (red), and $t_d = 114\frac{2}{3}$ (dashed) and $349\frac{2}{3}$ (solid). The vertical line and arrow indicate the homogeneous length scale λ_{hom} and the MLV center-to-center distance $2R_{MLV}$, respectively. The times are reported in units of the simulation time step dt. (For interpretation of the references to colour in this figure legend, the reader is referred to the web version of this article.)

To summarize, small-scale heterogeneity of the local spin density $\rho(\mathbf{r})$ and/or the local diffusion tensor $\mathbf{D}(\mathbf{r})$, both being structural properties of the material, gives rise to small-scale modulation of the COM spin density $\rho'(\mathbf{r},\delta)$ and, consequently,

the COM displacement probability $\overline{P'}(\mathbf{R}, t_d, \delta)$ when varying δ. In the PGSE experiment, the small-scale modulation of $\overline{P'}(\mathbf{R}, t_d, \delta)$ is detected as a variation of $E(q,t_d,\delta)$ at high q. From the maximum value of q for which $E(q,t_d,\delta)$ is independent of δ, the homogeneous length scale λ_{hom} can be inferred.

4. Materials and methods

4.1. Materials

Tri-ethylene glycol mono n-decyl ether ($C_{10}E_3$) with a purity higher than 99.8% was purchased from Nikko Chemical Co. (Tokyo, Japan). Deuterium oxide (D_2O) was obtained from Sigma Chemicals (Steinheim, Germany). Samples containing 40 wt% surfactant were prepared by weighing the desired amounts of surfactant and water into vials, mixing them in a vortex mixer and centrifuging them in order to remove air bubbles. All samples were prepared with D_2O as a probe for deuterium NMR spectroscopy. The residual protons in D_2O together with protons originating from the hydroxy group of the surfactant resulted in a signal sufficient for ^{1}H diffusion measurements as well. The samples were sheared in a Physica UDS 200 rheometer using the cone-and-plate geometry (MK22/M, 1° cone angle). The instrument is equipped with a temperature control unit that was calibrated to give a temperature in the sample chamber within 0.1 °C of the set value. A solvent trap was used to prevent water evaporation. MLVs were generated by applying a constant shear rate until reaching a steady state in viscosity. Then, the shear-induced MLVs were gently transferred to a 5 mm NMR tube with the help of a syringe. The mechanical stress imposed during this procedure is not high enough to destroy the MLVs and they maintain their integrity as confirmed by ^{2}H NMR. It should be noted, however, that the 'relaxed' MLV structure observed for our samples at rest might differ slightly from the MLV structure under shear, but a difference in the size of the MLVs is not expected. The structure under shear could be investigated using a rheo-NMR probe as in the investigations reported by Lutti and Callaghan [28–32].

The same sample was used for both ^{2}H spectroscopy and ^{1}H diffusometry. The two experiments were carried out immediately after each other to avoid sample changes.

4.2. NMR experiments

^{2}H NMR spectra were recorded at a magnetic field of 2.3 T on a Bruker DMX100 spectrometer operating at a ^{2}H resonance frequency of 15.35 MHz. Spectra were obtained by Fourier transformation of the signal following a single 90°-pulse of 10.5 μs. The temperature of the sample, which was controlled using an air-flow system, was set to 25 °C.

NMR diffusometry measurements were performed at 25 °C on a Bruker AVII-200 spectrometer operating at a resonance frequency of 200.13 MHz for ^{1}H. Gradient pulses with a maximum strength of 9.6 Tm^{-1} were generated by a Bruker DIFF-25 gradient probe controlled by a Great Master Unit. The water ^{1}H signal was recorded with a stimulated echo sequence [50] for an array of q-, t_d-, and δ-values as reported in Fig. 6. For each value of δ, the gradient strength was adjusted to yield the same range of q. The accuracy of this procedure was tested as described in Ref. [51].

5. Results and discussion

In the following we first present the results from ^{2}H NMR spectroscopy, yielding independent estimates of the MLV size. Subsequently we move on to the PGSE NMR results, first focusing on the long-range diffusion coefficient D_∞, and then the determination of the homogeneous length scale λ_{hom}. Finally, we compare our results with various estimates of the MLV size found in the literature.

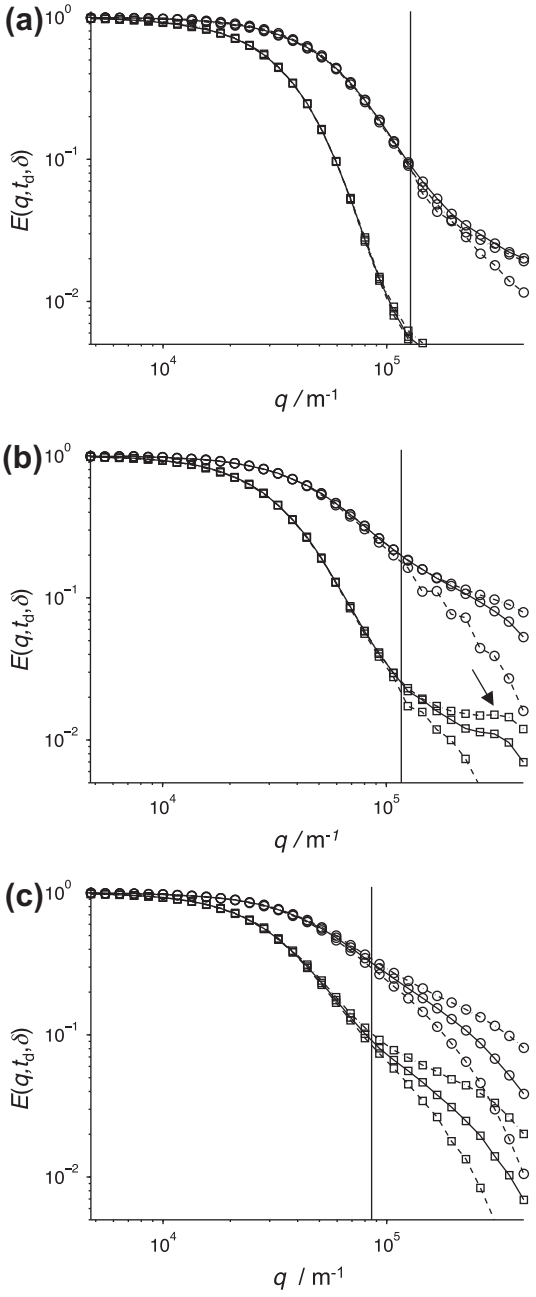

Fig. 6. Experimental PGSE signal $E(q,t_d,\delta)$ vs wave vector q for water in MLVs formed at the shear rates (a) 15, (b) 10, and (c) 5 s^{-1}, using the timing variables δ = 1 (dashed), 4.5 (solid), 20 ms (dash-dotted), and t_d = 40 (circles) and 118 ms (squares). The vertical lines indicate the homogeneous length scale λ_{hom} evaluated with a 1.1 threshold for the variation of $E(q,t_d,\delta)$ with δ. The arrow in (b) shows a Bragg peak related to the MLV center-to-center distance $2R_{MLV}$.

5.1. ^{2}H NMR spectroscopy

The ^{2}H NMR technique probes the motionally averaged electric quadrupole couplings between the deuterium nuclei (spin I = 1) and the electric field gradients at the sites of the observed nuclei [52].

When the D_2O molecules experience a macroscopically anisotropic environment the quadrupolar interaction has a non-zero average, generating a splitting of the signal into two peaks. In the

case of uniaxial symmetry, as is the case for the L_α phase, the ^{2}H spectrum consists of a doublet with a frequency separation $\Delta\nu$ given by [53]

$$\Delta\nu = \frac{3}{4}\delta_Q(3\cos^2\theta - 1), \tag{24}$$

where θ is the angle between the director (the symmetry axis of the phase) and the magnetic field, $\delta_Q = e^2\bar{q}Q/h$ is the motionally averaged quadrupole coupling constant, e is the elementary charge, $e\bar{q}$ is the largest principal value of the electric field gradient, Q is the nuclear quadropole moment and h is Planck's constant. According to Eq. (24), the deuterium NMR line shape depends on the distribution of director orientations. A disordered lamellar phase consisting of many domains of extended flat layers whose orientations are isotropically distributed in space gives rise to the characteristic line shape of a polycrystalline sample also known as powder or Pake pattern [54].

As long as the lamellae are planar the diffusive motion of the probe molecule D_2O has no extra rotational component besides the anisotropic local tumbling and the characteristic quadrupole coupling of the L_α phase is entirely given by the motional averaging caused by the local, ansiotropic motion. However, when the layers are curved, the preferred diffusion parallel to the layers is connected to a rotation and therefore leads to an additional motional narrowing of the spectrum. This results in a decrease and eventually a collapse of the quadrupolar splitting. Observing the transformation of the deuterium NMR line shape from a quadrupole doublet to a single peak can be used to monitor the formation of shear-induced MLVs in situ [14,26,55].

In this work shear was applied before the sample is filled into the NMR tube, and measurement of the ^{2}H NMR line shape is used as a means to monitor the morphology of the lamellar phase, on which the diffusion experiments are performed. A broad single deuterium line from the D_2O is observed for the three shear rates used in this study, confirming that the shear-induced MLVs have remained intact during the transfer to the NMR tubes. The line widths decrease with increasing shear rate, reflecting the shear-rate dependency of the vesicle radius: the vesicles become smaller when the shear rate is increased and smaller vesicles lead to narrower NMR bands [43]. In order to predict the vesicle radius from the spectra, one requires a model for the ^{2}H relaxation. Such a model was presented in Ref. [43]. This model assumes that the exchange of water between adjacent shells in an MLV is negligibly slow and that the vesicles are small enough for the NMR spectrum to be in the regime of isotropic motional narrowing. Each shell then yields a Lorentzian line whose width depends on the shell radii. Using this model on the present data the radius obtained for the shear rates 5, 10 and 15 s^{-1} were about 3.9, 2.7 and 1.8 μm, respectively. An alternative model would be to assume that the heavy water molecules sample all the layers. For such a case, the overall bandshape becomes Lorentzian. A fit of a Lorentzian band shape to the data, yields radii of 2.3, 1.7 and 1.3 μm for shear rates of 5, 10 and 15 s^{-1}, respectively. In fact, the calculations show that the situation in the shear-induced MLVs studied here lies between these two extreme cases. It is beyond the scope of this paper to develop a more realistic model in which the water molecules sample a few water layers.

In conclusion, the ^{2}H NMR line shapes obtained show similar features to those presented previously [43], showing that the integrity of the onions were preserved when the samples were tranferred to the NMR tubes, and that the diffusion experiments indeed were carried out on shear-induced MLVs.

5.2. PGSE NMR

The experimental PGSE NMR results are displayed in Fig. 6. In agreement with the simulation results in Fig. 5c, the range of q can be separated into two regions with respect to the behavior of the PGSE signal $E(q, t_d, \delta)$ when varying the effective diffusion time t_d and the gradient pulse length δ. For the origin of the different behaviors, see the discussion of the simulation results above.

We first consider the long-time diffusion coefficients of water in the MLV systems D_∞. These can, as noted above, be obtained from the echo intensities at low q-values. Using the initial decay (E values of 0.9–1, generally the first five to ten data points), the obtained value for D_∞ was $1.7 \pm 0.06 \times 10^{-10}$ m^2 s^{-1}, for all samples and diffusion times. Since there is no dependence of D_∞ on the diffusion times, the long-time limit has been reached. We note that the long-range diffusion coefficients are independent of the onion radius.

To rationalize these findings we use the cell-model approach put forth by Jönsson et al. [56]. Consider the system depicted in Fig. 7. It consists of a sphere embedded in a different medium. The volume fraction of the enclosed central region is Φ. D_i and C_i denote the diffusion coefficient and concentration of molecules, respectively, in region i. The effective (or long-time) diffusion in a system as in Fig. 7 is given by:

$$D_\infty = D_2 \frac{1}{1 - \left(1 - \frac{C_1}{C_2}\right)\Phi} \frac{1 - \beta\Phi}{1 + \frac{\beta\Phi}{2}} \tag{25}$$

where β is given by:

$$\beta = \frac{D_2C_2 - D_1C_1}{D_2C_2 + \frac{D_1C_1}{2}}. \tag{26}$$

Clearly, the effective diffusion coefficient is given by the solubilities and the diffusion coefficients in the two regions as well as the volume fraction of each region. The model defined by Eqs. (25) and (26) can now be extended to treat also multilamellar vesicles. This is done by assuming that there is a central water core in the onion, and that successive concentric shells of bilayers and water are added step by step. First, the effective diffusion coefficient is calculated for a system with a water core surrounded by a single bilayer (as in Fig. 7) using Eqs. (25) and (26) above. Then an effective concentration of water is calculated for this entire system by dividing the total amount of water in the system by the total volume. In the next step, the entire system with its effective values of D and C is taken as the enclosed region 1, a layer of water is added as region 2, and the calculation is repeated to obtain D and C for this enlarged system. The process is then repeated successively after addition of each shell of bilayer and water, respectively. The result of such a calculation is given in Fig. 8, with the parameter values given in the caption.

With only a few layers the long-time diffusion depends substantially on whether the outer layer is water or a bilayer; the diffusion being much faster if the outer layer is water. This result is

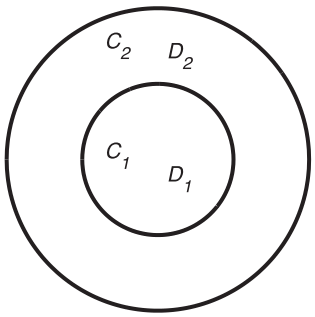

Fig. 7. Illustration of the parameters used in the cell-model approach for calculating the long-time diffusion coefficient D_∞. A region 1, with concentration C_1 and local diffusion coefficient D_1, is enclosed in an outer medium 2, with concentration C_2 and diffusion coefficient D_2.

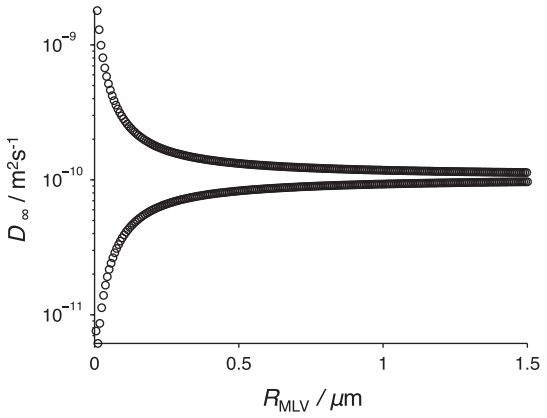

Fig. 8. Theoretical long-range diffusion coefficient D_∞ of water in an MLV system as a function of MLV radius R_{MLV} calculated with the cell-model approach as described in the text. The parameters used are: $C_1 = 30$ M, $D_1 = 1 \times 10^{-9}$ m^2 s^{-1}, and $C_2 = 20$ mM, $D_2 = 2 \times 10^{-9}$ m^2 s^{-1}. The inner water core is taken to have a radius of 25 Å, while the bilayer thickness is 25 Å and the thickness of the water shell is 40 Å. Each circle corresponds to the addition of a layer of either water or a bilayer. Depending on the type of the outermost layer the calculated diffusion coefficient is either on the upper (water) or lower curve (bilayer).

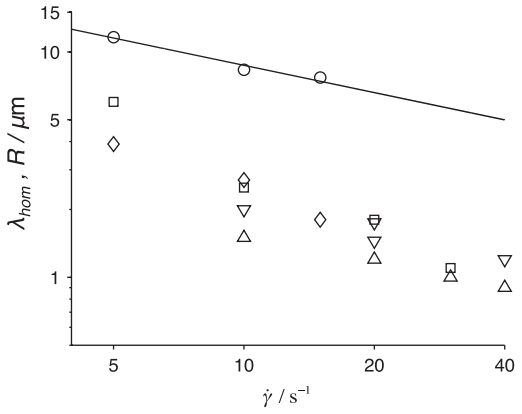

Fig. 9. Experimentally determined MLV radius R_{MLV} and homogeneous length scale λ_{hom} vs. shear rate $\dot{\gamma}$. Data is taken from this study (λ_{hom} from PGSE NMR ○, R_{MLV} from ^{2}H NMR ◇) and the literature (R_{MLV} from light scattering □ [23] ▽ [24] or ^{2}H NMR △ [43]). Errors in R_{MLV} are typically between 10% and 25%; the scattering is mainly due to variations in the mechanical history of the samples. Note that only the PGSE results (○) are presented as λ_{hom} whereas all other data points represent values of R_{MLV}. The solid line indicates a fit of $\lambda_{hom} = \beta\dot{\gamma}^\alpha$ to the λ_{hom} data, yielding $\alpha = -0.4$ (see Table 1).

expected. For instance, a system with two added layers, i.e. a water core surrounded by a bilayer and finally a water shell, represents a single wall vesicle with a vesicle volume fraction of 0.17 for the parameters defined in the caption to Fig. 8. Here the diffusion coefficient is only slightly reduced from the bulk value used (D_1 in Fig. 7). As the number of layers increases the water diffusion depends less on whether the outer layer is water or bilayers and also less on the total size (i.e. the number of shells added) of the onion. This is due to the fact that the effective diffusion coefficient in the interior (i.e. the volume surrounded by the outermost layer) reaches a steady state, while the volume fraction of the outer layer becomes very small. For the parameter values used to obtain the data in Fig. 8, the diffusion coefficient calculated for a 1.5 μm onion is 1.1×10^{-10} m^2 s^{-1} with water as the outer layer and approximately 10 % smaller if the outer shell is a bilayer. Thus the model calculation gives a slightly smaller value than the experimentally obtained value of D_∞. Given the uncertainty in the parameter values, this is perhaps not surprising. The model does however predict that the long-time diffusion of water is independent of the onion size.

Returning to Fig. 6, we now consider the region of high q in which the PGSE signal $E(q,t_d,\delta)$ depends on δ. For the shear rate of 10 s^{-1}, $E(q,t_d,\delta)$ features a shoulder at $q \approx 3.5 \times 10^5$ m^{-1} for $\delta =$ 20 ms and $t_d =$ 118 ms as indicated by the arrow in Fig. 6b. As previously discussed for the simulations, Bragg peaks can be expected to occur for locally ordered materials at favorable combinations of t_d and δ. The main reasons for just a small shoulder appearing (instead of a maximum) is, apart from the choice of time parameters, the fact that for a periodic three-dimensional array of onions (cf, Fig. 1 or the real system) more than one characteristic distance occurs in the direction of the measured diffusion when all lattice vectors are projected onto this direction. Based on these considerations we can regard the shoulder as a Bragg peak and derive from it an MLV radius of about 1.5 μm for the shear rate of 10 s^{-1}. There are a few possible reasons for the absence of a Bragg peak at the other shear rates, apart from an inadequate choice of time parameters. For the highest shear rate, 15 s^{-1}, the MLVs are probably too small to observe a maximum within the q-range used in these experiments. For the lowest shear rate, 5 s^{-1}, the missing maximum could be caused by a less ideal structure, for example, polydisperse MLVs or an incomplete transformation of planar lamellae into MLVs at this low shear rate.

Table 1
Exponent α obtained from fitting λ_{hom}, $R_{MLV} \propto \dot{\gamma}^\alpha$ to the data shown in Fig. 9.

Technique	α
Light scattering [23]	−1.0
Light scattering [24]	−0.4
^{2}H line shape [43]	−0.4
λ_{hom}	−0.4
^{2}H line shape	−0.6

While the Bragg peak can be expected to occur only in very favorable circumstances, a clear dependence of the size of the MLVs on shear-rate can be inferred from the more easily estimated λ_{hom}, as shown with vertical lines in Fig. 6. For the high shear rate λ_{hom} is 7.7 μm, for the intermediate shear rate it is 8.3 μm and for the low shear rate it is 12 μm. With increasing shear rate, λ_{hom} is decreasing in agreement with the ^{2}H NMR results and previous observations [2,23,40].

The shoulder in Fig. 6b is located at $q \approx 3/\lambda_{hom}$. As previously verified by simulations [37], λ_{hom} is directly proportional to the length of the periodicity of a microheterogeneous medium. Based on the data in Fig. 6, we assume a ratio of 3 between λ_{hom} and the vesicle diameter $2R_{MLV}$. Hence we can estimate the R_{MLV} from λ_{hom} even if no Bragg peak can be observed. Such a procedure yields $R_{MLV} = 1.4$, 1.5, and 2.0 μm for the shear rates of 15, 10, and 5 s^{-1}.

A comparison between literature data and our estimate of λ_{hom} is made in Fig. 9. As expected, λ_{hom} is consistently larger than R_{MLV} and follows the same trend when varying the shear rate $\dot{\gamma}$. According to theory, R_{MLV} depends on $\dot{\gamma}$ as $R_{MLV} \propto \dot{\gamma}^{-0.5}$ [3]. As can be seen in Table 1, keeping in mind the limited number of data points, λ_{hom} determined with PGSE NMR follows the expected relation to the same extent as light scattering and ^{2}H NMR lineshape analysis.

6. Conclusions

In this paper we have for nonionic surfactant MLV systems produced at different shear rates applied a recent PGSE NMR protocol for determining the homogeneous length scale λ_{hom}. Brownian dynamics simulations showed that the PGSE NMR Bragg peak observed for a well-ordered MLV system is related to the center-to-center distance between adjacent MLVs. Comparison with literature

data and theory indicated that λ_{hom} displays the expected scaling behavior with respect to the shear rate of formation. We anticipate λ_{hom} to become a useful, model-independent measure of the structural length scale of microheterogeneous media in general, especially so for systems not displaying PGSE NMR or small-angle light scattering Bragg peaks due to less well developed micrometer-scale order.

Acknowledgments

Felix Kleinschmidt is acknowledged for the experimental data which initiated this project. This work is financially supported by the Swedish Foundation for Strategic Research (SSF) and the Swedish Research Council (VR) through the Linnaeus Center of Excellence on Organizing Molecular Matter (OMM). The Colloid Group in Coimbra University is supported by grants from Fundação para a Ciência e Tecnologia (FCT) (Projects ref: POCTI/QUI/45344/2002 and POCTI/QUI/58689/2004). Bruno Medronho thanks FCT (Project ref: SFRH/BD/21467/2005).

References

[1] O. Diat, D. Roux, Preparation of monodisperse multilayer vesicles of controlled size and high encapsulation ratio, J. Phys. II France 3 (1993) 9–14.
[2] O. Diat, D. Roux, F. Nallet, Effect of shear on a lyotropic lamellar phase, J. Phys. II France 3 (1993) 1427–1452.
[3] D. Roux, F. Nallet, O. Diat, Rheology of lyotropic lamellar phases, Europhys. Lett. 24 (1993) 53–58.
[4] W. Richtering, Rheology and shear induced structures in surfactant solutions, Curr. Opin. Colloid Interface Sci. 6 (2001) 446–450.
[5] K. Mortensen, Structural studies of lamellar surfactant systems under shear, Curr. Opin. Colloid Interface Sci. 6 (2001) 140–145.
[6] P. Butler, Shear induced structures and transformations in complex fluids, Curr. Opin. Colloid Interface Sci. 4 (1999) 214–221.
[7] M.G. Berni, C.J. Lawrence, D. Machin, A review of the rheology of the lamellar phase in surfactant systems, Adv. Colloid Interface Sci. 98 (2002) 217–243.
[8] S. Fujii, T. Isojima, N. Sasaki, K. Kubota, M. Nakata, Shear-induced structural transformation of pentaethylene glycol n-dodecyl ether and lithium perfluorooctane sulfonate mixed-surfactant lamellar solutions, Colloid Polym. Sci. 281 (2003) 439–446.
[9] D. Burgemeister, C. Schmidt, Shear flow of lamellar polymer surfactants, Prog. Colloid Polym. Sci. 121 (2002) 95–100.
[10] J. Penfold, E. Staples, I. Tucker, J. Hubbard, L. Soubiran, A. Creeth, The effects of shear and co-surfactants on the evolution of the micro-structure in concentrated di-chain cationic surfactant solutions, Fibre Diffr. Rev. 11 (2003) 68–74.
[11] G. Montalvo, M. Valiente, A. Khan, Shear-induced topology changes in liquid crystals of the soybean lecithin/DDAB/water system, Langmuir 23 (2007) 10518–10524.
[12] Z. Yuan, S. Dong, W. Liu, J. Hao, Transition from vesicle phase to lamellar phase in salt-free catanionic surfactant solution, Langmuir 25 (2009) 8974–8981.
[13] Y. Kosaka, M. Ito, Y. Kawabata, T. Kato, Lamellar-to-onion transition with increasing temperature under shear flow in a nonionic surfactant/water system, Langmuir 26 (2010) 3835–3842.
[14] S. Müller, C. Börschig, W. Gronski, C. Schmidt, D. Roux, Shear-induced states of orientation of the lamellar phase of $C_{12}E_4$/water, Langmuir 15 (1999) 7558–7564.
[15] T.D. Le, U. Olsson, K. Mortensen, Packing states of multilamellar vesicles in a nonionic surfactant system, Phys. Chem. Chem. Phys. 3 (2001) 1310–1316.
[16] J. Leng, F. Nallet, D. Roux, Anomalous elasticity of an ordered lamellar liquid foam, Eur. Phys. J. E 4 (2001) 337–341.
[17] A.S. Wunenburger, A. Colin, J. Leng, A. Arnéodo, D. Roux, Oscillating viscosity in a lyotropic lamellar phase under shear flow, Phys. Rev. Lett. 86 (2001) 1374–1377.
[18] Y. Suganuma, M. Imai, T. Kato, U. Olsson, T. Takahashi, Order-disorder transition of nonionic onions under shear flow, Langmuir 26 (2010) 7988–7995.
[19] T. Gulik-Krzywicki, J.C. Dedieu, D. Roux, R. Degert, C. Laversanne, Freeze-fracture electron microscopy of sheared lamellar phase, Langmuir 12 (1996) 4668–4671.
[20] G.H. Sagar, M.A. Arunagirinathan, J.R. Bellare, Self-assembled surfactant nanostructures important in drug delivery: A review, Indian J. Exp. Biol. 45 (2007) 133–159.
[21] J. Zipfel, F. Nettesheim, P. Lindner, T.D. Le, U. Olsson, W. Richtering, Cylindrical intermediates in a shear-induced lamellar-to-vesicle transition, Europhys. Lett. 53 (2001) 335–341.
[22] L. Courbin, J.P. Delville, J. Rouch, P. Panizza, Instability of a lamellar phase under shear flow: formation of multilamellar vesicles, Phys. Rev. Lett. 89 (2002) 148305.
[23] F. Nettesheim, J. Zipfel, U. Olsson, F. Renth, P. Lindner, W. Richtering, Pathway of the shear-induced transition between planar lamellae and multilamellar vesicles as studied by time-resolved scattering techniques, Langmuir 19 (2003) 3603–3618.
[24] B. Medronho, S. Fujii, W. Richtering, M.G. Miguel, U. Olsson, Reversible size of shear-induced multi-lamellar vesicles, Colloid Polym. Sci. 284 (2005) 317–321.
[25] T. Kato, K. Miyazaki, Y. Kawabata, S. Komura, M. Fujii, M. Imai, Shear-induced structural transition in a lyotropic lamellar phase studied using small angle neutron and light scattering, J. Phys.: Condens. Matter 17 (2005) S2923–2928.
[26] B. Medronho, S. Shafaei, R. Szopko, M.G. Miguel, U. Olsson, C. Schmidt, Shear induced transitions between a planar lamellar phase and multilamellar vesicles: continuous versus discontinuous transformation, Langmuir 24 (2008) 6480–6486.
[27] S. Koschorek, S. Fujii, P. Lindner, W. Richtering, Multilamellar vesicles (onions) under shear quench: pathway of discontinuous size growth, Rheol. Acta 48 (2009) 231–240.
[28] A. Lutti, P.T. Callaghan, Undulations and fluctuations in a lamellar phase lyotropic liquid crystal and their suppression by weak shear flow, Phys. Rev. E 73 (2006) 011710.
[29] A. Lutti, P.T. Callaghan, Measurement of diffusion in the presence of shear flow, J. Magn. Reson. 180 (2006) 83–92.
[30] A. Lutti, P.T. Callaghan, Measurement of multilamellar onion dimensions under shear using frequency domain pulsed gradient NMR, J. Magn. Reson. 187 (2007) 251–257.
[31] A. Lutti, P.T. Callaghan, Effect of shear on an onion texture, Eur. Phys. J. E 24 (2007) 129–137.
[32] A. Lutti, P.T. Callaghan, Using solvent diffusion as a probe to characterize lamellar systems, Appl. Magn. Reson. 33 (2008) 293–310.
[33] P. Callaghan, Principles of Nuclear Magnetic Resonance Spectroscopy, Oxford Press, Oxford UK, 1991.
[34] W.S. Price, NMR Studies of Translational Motion, Cambridge University Press, 2009.
[35] D. Topgaard, Probing biological tissue microstructure with magnetic resonance diffusion techniques, Curr. Opin. Colloid Interface Sci. 11 (2006) 7–12.
[36] P.T. Callaghan, M.A. LeGros, D.N. Pinder, The measurement of diffusion using deuterium pulsed field gradient nuclear magnetic resonance, J. Chem. Phys. 79 (1983) 6372–6381.
[37] I. Åslund, C. Cabaleiro-Lago, O. Söderman, D. Topgaard, Diffusion NMR for determining the homogeneous length-scale in lamellar phases, J. Phys. Chem. B 110 (2008) 2782–2794.
[38] J.E. Spowart, B. Maruyama, D.B. Miracle, Multi-scale characterization of spatially heterogeneous systems: Implications for discontinuously reinforced metal-matrix composite microstructures, Mater. Sci. Eng. A 307 (2001) 51–66.
[39] J. Bear, Dynamics of Fluids in Porous Media, Dover Publications, New York, 1988.
[40] C. Oliviero, L. Coppola, R. Gianferri, I. Nicotera, U. Olsson, Dynamic phase diagram and onion formation in the system $C_{10}E_3/D_2O$, Colloids Surf. A 228 (2003) 85–90.
[41] F. Nettesheim, U. Olsson, P. Lindner, W. Richtering, Effect of flow reversal on the shear-induced formation of multilamellar vesicles, J. Phys. Chem. B 108 (2004) 6328–6335.
[42] S. Fujii, W. Richtering, Size and viscoelasticity of spatially confined multilamellar vesicles, Eur. Phys. J. E 19 (2006) 139–148.
[43] B. Medronho, C. Schmidt, U. Olsson, M.G. Miguel, Size determination of shear-induced multilamellar vesicles by rheo-NMR spectroscopy, Langmuir 26 (2010) 1477–1481.
[44] P. Stilbs, Fourier transform pulsed-gradient spin-echo studies of molecular diffusion, Prog. Nucl. Magn. Reson. Spectrosc. 19 (1987) 1–45.
[45] P.P. Mitra, B.I. Halperin, Effects of finite gradient-pulse widths in pulsed-field-gradient diffusion measurements, J. Magn. Reson. A 113 (1995) 94–101.
[46] P.P. Mitra, P.N. Sen, L. Schwartz, P. LeDoussal, Diffusion propagator as a probe of the structure of porous media, Phys. Rev. Lett. 68 (1992) 3555–3558.
[47] P.T. Callaghan, Pulsed-gradient spin-echo NMR for planar, cylindrical and spherical pores under conditions of wall relaxation, J. Magn. Reson. A 113 (1995) 53–59.
[48] P.P. Mitra, P.N. Sen, L.M. Schwartz, Short-time behavior of the diffusion coefficient as a geometrical probe of porous media, Phys. Rev. B 47 (1993) 8565–8574.
[49] O. Söderman, B. Jönsson, Restricted diffusion in cylindrical geometry, J. Magn. Reson. A 117 (1995) 94–97.
[50] J.E. Tanner, Use of stimulated echo in NMR-diffusion studies, J. Chem. Phys. 525 (1970) 2523–2526.
[51] C. Malmborg, M. Sjöbeck, S. Brockstedt, E. Englund, O. Söderman, D. Topgaard, Mapping the intracellular fraction of water by varying the gradient pulse length in *q*-space diffusion MRI, J. Magn. Reson. 180 (2006) 280–285.
[52] A. Abragam, Principles of Nuclear Magnetism, Clarendon, Oxford, UK, 1961.
[53] B. Halle, H. Wennerström, Interpretation of magnetic-resonance data from water nuclei in heterogeneous systems, J. Chem. Phys. 75 (1981) 1928–1943.
[54] G.E. Pake, Nuclear resonance absorption in hydrated crystals: fine structure of the proton line, J. Chem. Phys. 16 (1948) 327–336.
[55] M. Lukaschek, S. Müller, A. Hansenhindl, D.A. Grabowski, C. Schmidt, Lamellar lyomesophases under shear as studied by deuterium nuclear magnetic resonance, Colloid Polym. Sci. 274 (1996) 1–7.
[56] B. Jönsson, H. Wennerström, P.G. Nilsson, P. Linse, Self-diffusion of small molecules in colloidal systems, Colloid Polym. Sci. 264 (1986) 77–88.